Microbial strong organic ligand production is tightly coupled to iron in hydrothermal plumes

Colleen L. Hoffman[1,2,3*†] and Patrick J. Monreal[3,4*†], Justine B. Albers[5], Alastair J.M. Lough[6], Alyson E. Santoro[5], Travis Mellett[3,7], Kristen N. Buck[7,8], Alessandro Tagliabue[9], Maeve C. Lohan[6], Joseph A. Resing[1,2,3], Randelle M. Bundy[3]

[1]Joint Institute for the Study of Atmosphere and Ocean, University of Washington, 3737 Brooklyn
        Avenue NE, Seattle, WA 98195, USA
[2]Cooperative Institute for Climate, Ocean, and Ecosystem Studies, University of Washington,
        3737 Brooklyn Avenue NE, Seattle, WA 98195, USA
[3]School of Oceanography, University of Washington, 1501 NE Boat Street, Seattle, WA 98195,
        USA
[4]Earth Systems Program, Stanford University, 473 Via Ortega, Stanford, CA 94305,
        USA
[5]Department of Ecology, Evolution, and Marine Biology, University of California, Santa Barbara,
        CA 93106, USA
[6]Department of Ocean and Earth Sciences, National Oceanography Centre, University of
        Southampton, European Way, Southampton SO14 3ZH, United Kingdom
[7]College of Marine Science, University of South Florida, 140 7th Avenue South, St. Petersburg,
        FL, 33701, USA
[8]College of Earth, Oceans, and Atmospheric Sciences, Oregon State University, 2651 SW Orchard Ave,
        Corvallis, OR, 97331, USA
[9]Department of Earth, Ocean, and Ecological Sciences, University of Liverpool, 4 Brownlow
        Street, Liverpool l69 3GP, United Kingdom

†These authors contributed equally and should be considered co-first authors
*Correspondence: Colleen L. Hoffman and Patrick J. Monreal

Email: clhoffma@gmail.com, pmonreal@uw.edu

Abstract. Hydrothermal vents have emerged as an important source of iron to seawater, yet only a subset of this iron is soluble and persists long enough to impact the deep ocean iron inventory. The longevity and solubility of iron in seawater is in part governed by strong organic ligands, like siderophores, that are produced by microorganisms and are a part of the ocean's dissolved organic iron-binding ligand pool. These ligands have been hypothesized to aid in the persistence of dissolved iron in hydrothermal environments. To explore this hypothesis, we measured iron and iron-binding ligands including siderophores from 11 geochemically distinct sites along a 1,700 km section of the Mid-Atlantic Ridge. Siderophores were found in hydrothermal plumes at all sites, with proximity to the vent playing an important role in dictating siderophore type and diversity. The notable presence of amphiphilic siderophores may point to microbial utilization of siderophores to access particulate hydrothermal iron, and the exchange of dissolved and particulate iron. The tight coupling between strong ligands and dissolved iron within neutrally buoyant plumes across distinct hydrothermal environments, and the presence of dissolved siderophores with siderophore-producing microbial genera, suggests that biological production of ligands exerts a key control on hydrothermal dissolved iron concentrations.

1. Introduction

Over the last few decades, observations and modelling efforts have increased our understanding about the critical role organic ligands play in the cycling, transport, and utilization of trace metals (Tagliabue et al., 2017; Buck et al., 2018; Bundy et al., 2018; Moore et al., 2021). Iron (Fe) binding organic ligands in seawater have a wide range of sources, which are only just beginning to be understood. Recent observations suggest that microbial production of siderophores, humic-like substances and exopolysaccharides are some of the major contributors of marine organic ligands (Hassler et al., 2017), and links microbial activity to influence Fe cycling in environments ranging from hydrothermal plumes (Cowen and Bruland, 1985; Cowen et al., 1990) to the open ocean (Lauderdale et al., 2020). Strong Fe-binding organic ligands (L_1) are a heterogeneous mixture of microbially produced compounds that are operationally classified based on their binding strength with Fe (defined as $\log K_{Fe',FeL}^{cond} > 12$). They are thermodynamically favored to complex and stabilize external sources of Fe to prevent its scavenging and removal. As an example, in high Fe estuarine systems, only the dissolved Fe (dFe) bound to the strongest Fe-binding ligands is protected from scavenging and remains in solution (Bundy et al., 2015; Buck et al., 2007).

Siderophores are the strongest known Fe-binding organic ligands. They are produced by bacteria and fungi to facilitate Fe uptake and solubilize otherwise inaccessible phases in the marine environment (Butler, 2005; Manck et al., 2022). They have primarily been considered an important microbial strategy for Fe acquisition in the low Fe (dFe < 0.5 nM) surface ocean (Vraspir and Butler, 2009; Butler, 2005). However, siderophore uptake and biosynthesis genes were observed in >70% of Fe-related bacterial transcripts in a hydrothermal environment in Guaymas Basin (Li et al., 2014), have been identified in oxygen-deficient zones (Moore et

69   al., 2021), and are a common Fe acquisition strategy within terrestrial and pathogenic ecosystems (Sandy and

70   Butler, 2009), all of which are environments where Fe concentrations are orders of magnitude higher than

71   surface seawater.

72

73   Previous studies have both looked at unknown strong Fe-binding ligands besides siderophores in

74   hydrothermal plumes and throughout the deep ocean (Buck et al., 2018), as well as siderophores observed

75   below the euphotic zone (Bundy et al., 2018). However, no previous studies have ever directly measured

76   siderophores in hydrothermal systems. A 'stabilizing agent' (i.e. ligands) has been proposed for the long-

77   range transport of hydrothermal dFe into the ocean interior. The role of strong Fe-binding ligands in

78   hydrothermal dFe transport represents an important knowledge gap in how hydrothermal vents may impact

79   the ocean dFe inventory (Resing et al., 2015). Here, for the first time, we identified siderophores and

80   siderophore-producing microbes in 11 geochemically distinct hydrothermal environments along the slow-

81   spreading (20-50 mm/yr) Mid-Atlantic Ridge (MAR). Four black smokers (high temperature, high Fe), four

82   off-axis sites, one diffuse vent (low temperature, low Fe), one alkaline vent (pH 9-11, very low Fe), and one

83   non-vent fracture zone were investigated using both competitive ligand exchange-adsorptive cathodic

84   stripping voltammetry and state-of-the-art liquid chromatography coupled to electrospray ionization mass

85   spectroscopy (Boiteau et al., 2016) in a targeted approach to identify discrete components of the L_1 ligands

86   and to search for known siderophores. Microbial community analysis was also compared at three sites to

87   understand whether microbial ligand production impacts the supply of hydrothermal dFe to the ocean.

88   Overall, our results show microbially-produced siderophores were present in all sites, and that strong L_1

89   ligands were tightly coupled to hydrothermal dFe in the neutrally-buoyant plumes in this system. The

90   presence of organic ligands produced by bacteria in hydrothermal systems suggest that they play an important

91   role in deep ocean Fe cycling.

2. Results and Discussion

2.1 The role of iron-binding ligands in hydrothermal plumes

94   Strong organic Fe-binding ligands (defined here as L_1 ligands) have been found to be important in neutrally-

95   buoyant hydrothermal plumes (Tagliabue et al., 2017; Resing et al., 2015; Buck et al., 2018). But the

96   relationship between organic ligands and dFe have never been investigated together systematically across a

97   wide variety of vents in the same study. In this work, the average binding strength and concentration of

98   organic Fe-binding ligands were quantified in 11 vent systems that spanned a wide range in dFe

99   concentrations (0.41-90 nM) and underlying vent geology. Over 99% of dFe in the neutrally buoyant plumes

100   were complexed by L_1 ligands and the ligands were almost always completely saturated with dFe, meaning

101   Fe-free 'excess' L_1 ligands capable of binding additional Fe were present in low concentrations (< 1 nM; **Fig.

102   S1**). As a result, dFe concentrations were tightly coupled to L_1 ligands in a nearly 1:1 ratio (**Fig. 1d**), similar

103   to previous studies in other neutrally buoyant plumes (**Fig. 1e**) (Lough et al., 2022; Buck et al., 2018, 2015).

104   The strong coupling between dFe and ligands was only observed at sites where L_1 ligands were detected.

105   Some sampling locations, such as in the buoyant plume or closer to the vent orifice, contained high

106   concentrations of weaker ligands (log $K_{Fe',FeL}^{cond} < 12$, **Table S2**) with no correlation to dFe. This is consistent

107   with these environments likely being dominated by inorganic forms of Fe as hydrothermal fluids initially

108   mix with oxygenated seawater.

109

110   Our results indicate that L_1 ligands cap the dFe concentration in neutrally buoyant plumes. A similar control

111   on dFe concentrations by L_1 ligands has been previously observed in estuaries (Buck et al., 2007) and aerosol

112   solubility experiments (Fishwick et al., 2014). One possible explanation is that both the dFe and L_1 ligands

113   originate from the vent fluids themselves, yielding a tightly coupled hydrothermal endmember. However, the

114   concentration of L_1 ligands did not correlate with excess mantle Helium-3 ($^3He_{xs}$, **Fig S2**, **Table S2**) (Lough

115   et al., 2022), a nearly conservative tracer of the mixing of hydrothermal fluids with seawater (Buck et al.,

116   2018), and our samples closer to the vent source were dominated by weaker organic ligands showing no

117   correlation to dFe. This suggests the L_1 ligands were not directly sourced from the vent fluids along with dFe.

118   Another explanation is the source of L_1 ligands observed in the neutrally-buoyant plume are either from

119   bacteria that produced them in surrounding deep ocean seawater that was then entrained, local production

120   from vent-biota and/or microbial mats, diffusion from microbial production in sediments, or *in-situ*

121   production by bacteria within the neutrally buoyant plume (Mellett et al., *submitted*).

122

123   **2.2 The presence of siderophores in hydrothermal systems**

124   Siderophores were measured in a subset of the samples to further explore the source of the L_1 ligands coupled

125   to dFe in the neutrally-buoyant plume. Marine organic ligand composition changes with environmental

126   gradients (Boiteau et al., 2016; Gledhill and Buck, 2012), making the structure and functional groups of

127   siderophores identified in hydrothermal samples of particular interest. Somewhat surprisingly, siderophores

128   were found in all samples and we observed a large diversity of siderophores with high confidence using mass-

129   to-charge ratio (*m/z*), MS/MS spectra, and specific chromatographic characteristics (**Fig. 2a**). On-axis

130   spreading centers contained the highest dFe concentrations (> 20 nM) and wider variety of siderophores than

131   samples from fracture zones, diffuse, and off-axis sites (dFe $\leq$ 1 nM). The greatest number of distinct

132   siderophores were identified at Lucky Strike, Broken Spur, Rainbow, and TAG (**Fig. 2**). On average, 13

133   compounds were identified with high confidence per on-axis spreading center sample, compared with 5 per

134   diffuse/fracture zone sample, and 2.5 per off-axis sample (**Fig. 2b, Fig. S4**). Mixed-type siderophores —

135   containing different moieties that bind to Fe(III) — were common at all sites. Hydroxamates were identified

136   at and around spreading centers, yet none of these were detected with high confidence in samples from

137   diffuse/fracture zones (**Fig. S4**). Summed siderophore abundance in neutrally-buoyant plumes above

138   spreading centers was similarly more than twice that of samples from fracture zones or off-axis (**Fig. 2c**).

139   Thus, vent type and proximity played a role in the diversity and abundance of siderophore types observed,

140   likely related to the diversity of the microbial community and/or unique Fe acquisition strategies across sites.

141

142 Siderophores are operationally part of the L_1 ligand pool based on their binding strength (Gledhill and Buck,

143 2012) and patterns in their distributions reflected those of the strong ligands. The peak areas of each putative

144 siderophore we identified were used as a proxy for concentrations (*section 3.3*), and these concentrations

145 significantly correlated with dFe, as observed with dFe and L_1 ligands (**Fig. 2b**). Siderophores were present

146 in concentrations similar to the surface ocean (Boiteau et al., 2016; Moore et al., 2021; Park et al., 2022;

147 Bundy et al., 2018), and comprised 0.01-0.4% of the total L_1 ligands (**Table 1**). This is likely a substantial

148 underestimate of siderophore contributions to the L_1 ligand pool due to analytical constraints in identifying

149 unknown siderophores. Recent work on siderophore biosynthesis pathways and advances in genome mining

150 suggest that known siderophores represent a small fraction of what is expected to be produced in nature

151 (Hider and Kong, 2010; Reitz et al., 2022). In addition, most siderophores are not commercially available to

152 use as standards, and individual siderophores have different ionization or extraction efficiencies. We

153 restricted our reporting to compounds only identified with very high confidence (**Fig 2a**, **S3**). The extraction

154 efficiency for the solid phase extraction technique is approximately 5-10% for bulk Fe-binding organics

155 (Bundy et al., 2018) and 40% for a siderophore standard (Waska et al., 2015). Employing both corrections

156 yields siderophore contributions to the total L_1 pool of 0.1-4% and 0.025-1%, respectively. We are inevitably

157 missing many naturally occurring unknown compounds. Regardless of the small percentage contribution to

158 total L_1 ligands, it is evident that microbially produced siderophores were ubiquitous across all vent sites and

159 had similar distributional patterns as L_1 ligands. The identification of siderophores — and their relationship

160 with dFe — provides compelling evidence that microbial production of ligands is responsible for at least

161 some portion of the tight coupling between L_1 and dFe in hydrothermal systems along the MAR.

162

163 The presence and diversity of siderophores identified in this system was surprising given the relatively high

164 Fe concentrations of hydrothermal environments, but some interesting patterns were observed. For example,

165 previous work has shown that low Fe surface waters have higher concentrations of amphiphilic siderophores

166 compared to high Fe coastal waters (Boiteau et al., 2016), and amphiphilic siderophores are less common in

167 terrestrial environments (Hider and Kong, 2010). Amphiphilic siderophores have long hydrocarbon tails that

168 can be embedded into the lipid bilayer of the bacterial cell membrane providing a mechanism to shuttle Fe

169 into the cell and prevent diffusive loss (Martinez et al., 2003). Amphiphilic siderophores comprised 57% of

170 the siderophores in our samples (**Fig. S5**), supporting the ubiquity of amphiphilic siderophores in marine

171 environments (Butler and Theisen, 2010). Amphiphilic siderophores were found in concentrations between

172 0.3-4.7 pM, with the highest found at Rainbow (**Fig. 2d**, **Table S5**). These concentrations were similar to

173 those observed in the upper ocean (Boiteau et al., 2016; Bundy et al., 2018; Boiteau et al., 2019). Marine

174 bacteria produce suites of amphiphilic siderophores as a way to adapt to the change in hydrophilicity in the

175 surrounding environment (Sandy and Butler, 2009; Homann et al., 2009). Amphiphilic siderophores in

176 plumes could be a way for bacteria to access Fe as they are physically transported and cope with strong

177 chemical gradients, similar to the production of multiple siderophores in terrestrial and pathogenetic systems

178 as a means to access inorganic particulate Fe for cellular uptake and storage (Hider and Kong, 2010).

179

180 **2.3 Microbial sources of siderophores in hydrothermal plumes**

181 The high diversity of siderophores across a huge range of hydrothermal vent systems revealed several

182 surprising aspects of Fe cycling. The biosynthesis of a siderophore is energy-intensive and is regulated by Fe

183 concentration in the surrounding environment (Rizzi et al., 2019). Siderophore presence suggests that bacteria

184 are producing these compounds despite the overall higher Fe concentrations in the deep ocean and within

185 hydrothermal plumes. Consistent with siderophore utilization in terrestrial ecosystems (Hider and Kong,

186 2010; Sandy and Butler, 2009), one hypothesis is that siderophore production is beneficial to bacteria in the

187 plumes for transforming Fe from otherwise inaccessible forms, such as particulate nanopyrites or Fe

188 oxyhydroxides. To explore microbial production of siderophores, we examined microbial community

189 composition around Rainbow (St. 11, 17) and Lucky Strike (St. 7; **Table 1, Table S1**) using 16S rRNA gene-

190 based amplicon sequencing to detect bacteria with the metabolic potential to synthesize siderophores (**Fig. 3,**

191 **S11**), where the presence of taxa encoding siderophore biosynthetic gene clusters indicates whether the

192 microbial community is genetically capable of producing the compounds we observed. Bacterial genera

193 containing known siderophore-producers were found at all three MAR sites examined, and putative

194 siderophore-producers represented 3-20% of the relative abundance of the community (**Fig. 3**). Putative

195 siderophore-producers were more abundant in the 3 µm (particle-attached) size fraction than in the 0.2 µm

196 (free-living) fraction, suggesting siderophore production is more common in particle-associated bacteria in

197 hydrothermal environments.

198

199 We found microbial genera in our samples that can produce a subset of the siderophores identified here,

200 including ferrioxamines, vibrioferrin, and acinetoferrin (Butler, 2005; Vraspir and Butler, 2009; Moore et al.,

201 2021; Bundy et al., 2018; Boiteau et al., 2016). Genera with the genetic potential to produce ferrioxamines

202 were present at all three sites, while those known to produce vibrioferrin were present at Lucky Strike and

203 Rainbow, and those producing acinetoferrin were also present at Rainbow (**Table S1, S6**). Mycobactins were

204 detected with high confidence in every sample of this study, and genes encoding mycobactin have been

205 detected in a cultured organism from a hydrothermal system (Gu et al., 2019), but no mycobactin producers

206 were identified in this study. We detected woodybactin D with high confidence in 5 out of 11 sites. Although

207 these biosynthetic genes were not identified in any of the genera observed, woodybactin D is a carboxylate

208 siderophore isolated from *Shewanella* (Carmichael et al., 2019), and groups of deep-sea *Shewanella* (Kato

209 and Nogi, 2001) were found in the dataset (**Fig. S11**). The biosynthesis genes for many of the siderophores

210 identified are unknown. Thus, finding genera capable of producing only a subset of the siderophores

211 characterized is not surprising. The observation that a significant portion of the *in-situ* microbial community

212 is capable of synthesizing siderophores (**Fig 3**) suggests that siderophore production is more widespread in
213 the deep ocean than previously believed.

214

215 **2.4 The impact of strong ligands and siderophores on dissolved iron in neutrally-buoyant plumes**

216 Evidence that siderophores are ubiquitous in the marine environment — including higher Fe environments
217 — has been increasing (Park et al., 2023). The high dFe associated with hydrothermal plumes may still not
218 be high enough to suppress siderophore production due to the elevated Fe requirements of heterotrophic
219 bacteria (Tortell et al., 1996). It is also likely that in hydrothermal plumes not all of the Fe is bio-accessible.
220 Soil microbes secrete siderophores to solubilize particulate Fe (Crowley et al., 1991) and similar processes
221 could be occurring in hydrothermal plumes, where Fe mineral phases associated with organic compounds are
222 common (Hoffman et al., 2020; Toner et al., 2009). Although our measurements suggest that dFe in the
223 neutrally-buoyant plume is dominated by organic complexation, the L_1 measurements alone cannot
224 distinguish between purely organic phases or a mixture of inorganic and organic ligands in complex
225 aggregations or small colloids. Given the evidence from particulate Fe studies in neutrally-buoyant plumes
226 (Hoffman et al. 2020), it is highly likely that some portion of what is detected in the L_1 pool is a mixture of
227 organic and inorganic Fe in small colloids which are operationally in the dFe pool (Fitzsimmons et al., 2017).
228 It is also telling that most siderophore-producing genera were found to be particle-associated (**Fig. 3**),
229 providing additional evidence that siderophores might be produced to solubilize particulate Fe or access other
230 colloidal phases. Further work that assesses why bacteria are producing siderophores in neutrally buoyant
231 plumes will be important for understanding microbial metabolism in these systems, and the impact of
232 siderophore production on Fe dispersal.

233

234 Organic Fe-binding ligands have been implicated in playing a critical role in the preservation and transport
235 of hydrothermal dFe into the ocean interior (Hoffman et al., 2018; Resing et al., 2015; Fitzsimmons et al.,
236 2017; Toner et al., 2009; Bennett et al., 2011, 2008; Buck et al., 2018; Sander and Koschinsky, 2011). In this
237 work, L_1 ligands were tightly coupled to dFe in neutrally buoyant plumes along the MAR and the presence
238 of siderophores in these samples provided evidence for the first time, that at least some of these ligands are
239 microbially produced. How these complexes may facilitate the exchange of Fe between dissolved and
240 particulate phases (Fitzsimmons et al., 2017), and whether siderophores are present across additional
241 hydrothermal vent systems will aid in constraining the biogeochemical importance of microbial feedbacks in
242 impacting the hydrothermal dFe supply to the deep ocean.

243

244 **3. Appendix: Materials and Methods**

245 **3.1 Sampling and cruise transect**

246 Samples were collected as part of the 2017-2018 U.K. GEOTRACES GA13 section cruise along the Mid-
247 Atlantic Ridge. Water samples from 11 venting and near venting locations were collected using a Seabird

248 911 conductivity, temperature, and depth (CTD) titanium rosette using conducting Kevlar wire with an
249 oxidation-reduction potential (ORP) sensor to detect plumes. Teflon coated OTE (Ocean Test Equipment)
250 bottles were pressurized to approximately 7 psi with 0.2 µm filtered air using an oil free compressor. A
251 Sartobran 300 (Sartorius) filter capsule (0.2 µm) was used to collect filtered seawater samples into clean 250
252 mL LDPE sample bottles. Bottles and caps were rinsed 3 times with the filtered sample before being filled.
253 Samples were stored frozen at -20˚C for Fe-organic ligand characterization by voltammetry and mass
254 spectrometry.

3.2 Fe-binding ligand concentration and binding strengths Competitive Ligand Exchange-Adsorptive Cathodic Stripping Voltammetry

257 Fe-binding ligand concentrations and binding strengths (defined as conditional binding constants, log $K^{cond}_{Fe',FeL}$
258 > 12) were determined by competitive ligand exchange-adsorptive cathodic stripping voltammetry (CLE-
259 ACSV) with a BAS*i* controlled growth mercury electrode (CGME) with an Ag/AgCl$^-$ reference electrode
260 and platinum auxiliary electrode (Bioanalytical Systems Incorporated). Using previously established
261 methods (Buck et al., 2015, 2018; Bundy et al., 2018; Abualhaija and van den Berg, 2014; Hawkes et al.,
262 2013b), 40 frozen filtrate (<0.2 µm) samples with dFe concentrations between 0.41-11.67 nM (**Table S1-**
263 **S2**) were thawed in a 4˚C fridge prior to analysis. A 15-point titration curve was analyzed for each sample.
264 Briefly, within each titration, every point sequentially received 10 mL of sample, 7.5 mM of borate-
265 ammonium buffer, 10 µM salicylaldoxime (SA) added ligand, and a dFe addition. Data was collected using
266 the *Epsilon Eclipse Electrochemical Analyzer* (v.213) with a deposition time of 120 seconds and analyzed
267 using *ElectroChemical Data Software* (v2001-2014) and *ProMCC* (v2008-2018) to determine peak areas and
268 Fe-binding ligand parameters, respectively. All results were confirmed to fall within the analytical window
269 of the method by comparing the side reaction coefficient of the added ligand α_{SA} to the side reaction
270 coefficient of the natural ligands detected (α_L). If the α_L was within an order of magnitude of α_{SA} then the
271 results were deemed to fall within the analytical window.

3.3 Reverse Titration-CLE-ACSV

273 Reverse titration-CLE-ACSV (RT-CLE-ACSV) (Hawkes et al., 2013a) was completed on 10 samples from
274 Broken Spur, and TAG hydrothermal vent fields with dFe concentrations between 19.01-90.25 nM (**Table**
275 **S1-S2**). Briefly, a 10-point titration curve was analyzed for each sample with each titration point consisting
276 of 10 mL of sample buffered with 7.5 mM boric acid and the competitive ligand 1-nitroso-2-napthol (NN)
277 additions. All samples were analyzed on a BAS*i* Controlled Growth Mercury Electrode (CGME) with the
278 *Epsilon Eclipse Electrochemical Analyzer* (v.213) and deposition time of 120 seconds. For each sample,
279 competitive ligand NN additions were 0.5, 1, 2, 3, 4, 6, 9, 15, 20, and 40 µM. Samples were equilibrated
280 overnight and purged with N$_2$ (99.99%) for 5 minutes before analysis. At the end of each titration, three Fe
281 additions (3-15 nM) were added to the final titration point to get the total concentration of Fe in equilibrium
282 with ligands. Data was analyzed using *ElectroChemical Data Software* (v2001-2014) to acquire peak areas

283   and a package in R using the model parameters of β_{FeNN3} = 5.12 x 10^{16}, χ_{min} = 0.8, χ_{max} = 0.9, and *c1high* =

284   0.75 to determine the Fe-binding ligand parameters (Hawkes et al., 2013a). These parameters were chosen

285   based on the recommendations for undersaturated samples and titrations curves where ip_{max} was not reached

286   (Hawkes et al., 2013a). All other parameters within the model we kept at the default values.

287   **3.4 Siderophore quantification and characterization**

288   In addition to measuring Fe-binding ligands by voltammetry, we also identified and quantified siderophores.

289   Between 0.65-1.5 L of 0.2 μm filtered seawater pooled from ligand samples at each site (described above)

290   was pumped slowly (15-20 mL min^{-1}) onto a polystyrene-divinylbenzene (Bond Elut ENV) solid phase

291   extraction (SPE) column (Bundy et al., 2018; Boiteau et al., 2016). SPE columns were rinsed with MilliQ

292   and stored at -20ºC until analysis. For the analytical measurements, samples were thawed in the dark, eluted

293   in 12 mL of distilled methanol, and dried down to between 0.2-0.5 mL of sample eluent (**Table S1**). Aliquots

294   were analyzed by reverse-phase liquid chromatography (LC) on a trace metal clean bio-inert LC (Thermo

295   Dionex 3000 NCS). The LC was interfaced with an electrospray ionization-mass spectrometer (ESI-MS;

296   Thermo Q-Exactive HF) to identify and quantify the compounds based on accurate mass (MS^1) and the

297   fragmentation (MS^2) data (Bundy et al., 2018; Boiteau et al., 2016). MSconvert (Proteowizard) was used to

298   convert MS data to an open source mzxML format, and two stages of data processing were conducted using

299   modified versions of previously reported R scripts (Bundy et al., 2018; Boiteau et al., 2016). In the first stage,

300   mzxML files were read into R using new package "RaMS" (Kumler and Ingalls, 2022) , and extracted ion

301   chromatograms (EICs) were generated for each targeted *m/z* of interest from an in-house database of

302   siderophores. The *m/z* targets were the ionized apo, ^{54}Fe-bound, and ^{56}Fe-bound version of each siderophore,

303   with a tolerance of 7.5 ppm. Putative siderophore candidates were filtered through a series of hard thresholds,

304   such that MS^1 spectra were quality controlled to contain a minimum of 25 datapoints and the maximum

305   intensity of each EIC was greater than 1e4 counts. Spectra meeting these criteria and containing either ^{54}Fe-

306   bound and ^{56}Fe-bound *m/z* peaks within 30 seconds of each other or an apo peak were displayed for the user

307   to further inspect peak quality and make the final decision of whether to move on to stage two of processing

308   with a given siderophore candidate.

309

310   Stage two of processing extracted MS^2 spectra of the apo and Fe-bound forms of candidate siderophores to

311   compare with the predicted MS^2 generated by *in silico* fragmenter MetFrag (Ruttkies et al., 2016). The *in*

312   *silico* fragmenter feature was run with a tolerance of 10 ppm on "$[M+H]^+$" and "$[M+Na]^+$" modes. A

313   confidence level of 1-4, from highest to lowest confidence, was then assigned to putative siderophores based

314   on the following criteria: (1) peaks were present in MS^1 and MS^2 spectra, and at least one of the three most-

315   intense MS^2 fragments matched *in silico* fragmentation, (2) peaks were present in MS^1 and MS^2 spectra, and

316   smaller-intensity fragments matched *in silico* fragmentation, (3) peaks were present in MS^1 and MS^2 spectra,

317   but little to no fragments matched *in silico* fragmentation, and (4) nicely shaped peaks were identified in MS^1

318   spectra but no MS^2 spectra was collected (outlined in **Table S4**; example spectra in **Fig. S6-S9**). The

319 confidence levels were modelled after reporting standards for metabolite identification (Sumner et al., 2007).
320 MetFrag pulls chemical structures from publicly-available databases like PubChem or COCONUT(Sorokina
321 et al., 2021), which contain most, but not all variations of siderophores. As such, Fe-bound candidates were
322 usually run against the apo form available in the database, and for siderophores with similar structures but
323 variations in fatty chain length or double bond placement, sometimes only one parent structure was available.
324
325 A 5-point standard curve with known concentrations of siderophore ferrioxamine E was used for
326 quantification of putative siderophores, with a limit of detection of 0.257 nM in the eluent (**Fig. S10**), or
327 0.07-0.21 pM in the sample depending on sample-to-eluent volume ratio at each site (**Table S1**). MS[1] peaks
328 were integrated for all putatively identified siderophores and peak areas were converted to concentration
329 using the standard curve and the concentration factor of sample volume to eluent volume (**Fig. S10**).
330 Commercial standards are not available for most siderophores, and different compounds have distinct
331 ionization efficiencies in ESI-MS. Thus, the siderophore concentrations reported here are estimates of
332 siderophore concentrations in these environments based on ferrioxamine E, chosen for its commercial
333 availability and use in prior studies (e.g., (Boiteau et al., 2016)). Additionally, 1 mM of cyanocobalamin was
334 added as an internal standard to each sample aliquot to address any changes in sensitivity during LC-ESI-MS
335 runs. All putative siderophores that were identified with peak areas less than the detection limit were
336 discarded, and all remaining putative compounds with at least confidence levels 1 and 2 at one site were
337 included in the manuscript and are referred to as siderophores throughout. Siderophore identifications remain
338 putative due to inherent uncertainty with assignments by mass, but the confidence levels were designed such
339 that high confidence candidates contain siderophore-like moieties in their fragments. Limited sample
340 volumes prevented analysis via LC-ICP-MS like previous studies, which, in addition to greater availability
341 of commercial standards and more analytical comparisons between ferrioxamine E with other siderophore
342 types, would allow definitive characterization in future studies. Confidence level 3 and 4 putative
343 siderophores are only included in the Supplementary Information (**Table S5**). In a final step of quality
344 control, EICs for ^{13}C isotopologues of candidates were inspected to verify matching peak structure.

345 **3.5 Microbial community analysis**

346 Microbial community composition was assessed in neutrally buoyant plumes and near venting sites at three
347 sites: Lucky Strike (Station 7; 1670 m), 10 km S of Rainbow (Station 17; 2000 m), and 200 km E of Rainbow
348 (Station 11; 600 m, 1600 m and 2250 m). A range of 1- 2 L of seawater were filtered by pressure filtration
349 through sequential 25 mm membrane filters housed in polypropylene filter holders (Whatman SwinLok, GE
350 Healthcare, Pittsburgh, Pennsylvania) using a peristaltic pump and silicone tubing. Samples first passed
351 through a 3 µm pore-size polyester membrane filter (Sterlitech, Auburn, Washington) then onto a 0.2 µm
352 pore-size polyethersulfone membrane filter (Supor-200, Pall Corporation, Port Washington, New York).
353 Pump tubing was acid washed with 10% hydrochloric acid and flushed with ultrapure water between each

354   sample. The filters were flash frozen in liquid nitrogen in 2 mL gasketed bead beating tubes (Fisher Scientific)

355   at sea.

356

357   Nucleic acids (DNA) were extracted as described previously(Santoro et al., 2010), with slight modifications.

358   Briefly, cells on the filters were lysed directly in the bead beating tubes with sucrose-ethylene diamine

359   tetraacetic acid (EDTA) lysis buffer (0.75 M sucrose, 20 mM EDTA, 400 mM NaCl, 50 mM Tris) and 1%

360   sodium dodecyl sulfate. Tubes were then agitated in a bead beating machine (Biospec Products) for 1 min,

361   and subsequently heated for 2 min. at 99°C in a heat block. Proteinase K (New England Biolabs) was added

362   to a final concentration of 0.5 mg/mL. Filters were incubated at 55°C for approximately 4 h and the resulting

363   lysates were purified with the DNeasy kit (Qiagen) using a slightly modified protocol (Santoro et al., 2010).

364   The purified nucleic acids were eluted in 200 μL of DNase, RNase-free water, and quantified using a

365   fluorometer (Qubit and Quanti-T HS reagent, Invitrogen Molecular Probes).

366

367   The 16S rRNA gene was amplified in all samples using V4 primers (Apprill et al., 2015; Parada et al., 2016)

368   (515F-Y and 806RB) following a previously established protocol (Stephens et al., 2020). Amplicons were

369   sequenced using a paired-end 250bp run on an Illumina MiSeq 500 and demultiplexed by the UC Davis

370   Genome Center. The resulting 16S rRNA amplicon sequences were filtered and trimmed using the DADA2

371   pipeline in R(Callahan et al., 2016). Taxonomic assignments were made with version 138.1 of the SILVA

372   SSU   database   (Quast   et   al.,   2013)   (silva_nr99_v138.1_wSpecies_train_set.fa.gz   ;

373   doi:10.5281/zenodo.4587955; accessed March 2022). Chloroplast and mitochondrial sequences were filtered

374   out of the dataset using the 'phyloseq' R package (v 1.38.0), after which samples had read depths ranging

375   from 9375 – 65486 reads (average 28425 ± 20014 reads) and represented 1010 unique amplicon sequence

376   variants (ASVs). Read counts were transformed from absolute to relative abundance and taxa were

377   aggregated to the Family level. The ten most abundant families present in each sample were visualized using

378   the 'ggplot2' package (v. 3.3.5).

379

380   In order to assess the potential of the observed prokaryotic taxa to produce siderophores, we downloaded all

381   siderophore biosynthetic gene clusters (BGCs) in the antismash secondary metabolite database ($n = 7909$)

382   and used text-string matching to compare genera containing these BGCs to the genera found in our 16S rRNA

383   gene dataset(Blin et al., 2021). We cross-referenced the nomenclature of antismash-predicted siderophores

384   with that of the siderophores identified by LC-ESI-MS in this study, accounting for minor differences in

385   naming convention between the two databases, to determine if microbial community members present at

386   each site were predicted to make any of the siderophores that were measured at that site. Station 38 and

387   Station 12 were the closest sites with siderophore measurements for comparison against the taxonomic

388   samples taken at 200 km E of Rainbow and 10 km S of Rainbow, respectively. Samples for microbial

389   taxonomy and siderophore identity were taken from the same location at Lucky Strike and thus directly

390   compared.

391

Data Availability

393 The CSV data reported in this study has been deposited at Zenodo under the DOI:
394 http://doi.org/10.5281/zenodo.7325154. The LC-ES-MS data has been deposited on Massive under the DOI:
395 http://doi.org/doi.10.25345/C5V97ZW7N. Microbial 16S rRNA data have been deposited on GenBank under
396 the accession number BioProject #PRJNA865382. All data is freely available on each of these data
397 repositories.

398

399

415

416 **Author Contributions:** Manuscript preparation, sample/data processing, CSV analysis, and interpretation
417 LC-ESI-MS data analysis and interpretation (C.L.H. and P.J.M.), microbial analysis and interpretation
418 (J.B.A. and A.E.S.), dissolved iron and derived excess $^3\text{He}_{xs}$ measurements, sample collection (A.J.M. L. and
419 M.C.L.), microbial data collection and ligand data interpretation (T.M. and K.N.B.), and project design and
420 planning, data interpretation, and mentoring (A.T., M.C.L., J.A.R., and R.M.B.). All authors were involved
421 in editing and revision of the manuscript.

422

423 **Competing Interest Statement:** The authors declare no competing interests.

424

References

426 Abualhaija, M. M. and van den Berg, C. M. G. G.: Chemical speciation of iron in seawater using catalytic

cathodic stripping voltammetry with ligand competition against salicylaldoxime, Mar. Chem., 164, 60–74, https://doi.org/10.1016/j.marchem.2014.06.005, 2014.

Apprill, A., Mcnally, S., Parsons, R., and Weber, L.: Minor revision to V4 region SSU rRNA 806R gene primer greatly increases detection of SAR11 bacterioplankton, Aquat. Microb. Ecol., 75, 129–137, https://doi.org/10.3354/ame01753, 2015.

Bazylev, B. A.: Allochemical Metamorphism of Mantle Peridoties in the Hayes Fracture Zone of the North Atlantic, Petrology, 5, 362–379, 1997.

Beaulieu, S. E. and Szafrański, K. M.: InterRidge Global Database of Active Submarine Hydrothermal Vent Fields Version 3.4, https://doi.org/10.1594/PANGAEA.917894, 2020.

Bennett, S. a., Achterberg, E. P., Connelly, D. P., Statham, P. J., Fones, G. R., and German, C. R.: The distribution and stabilisation of dissolved Fe in deep-sea hydrothermal plumes, Earth Planet. Sci. Lett., 270, 157–167, https://doi.org/10.1016/j.epsl.2008.01.048, 2008.

Bennett, S. a., Hansman, R. L., Sessions, A. L., Nakamura, K. ichi, and Edwards, K. J.: Tracing iron-fueled microbial carbon production within the hydrothermal plume at the Loihi seamount, Geochim. Cosmochim. Acta, 75, 5526–5539, https://doi.org/10.1016/j.gca.2011.06.039, 2011.

Blin, K., Shaw, S., Kautsar, S. A., Medema, M. H., and Weber, T.: The antiSMASH database version 3: Increased taxonomic coverage and new query features for modular enzymes, Nucleic Acids Res., 49, D639–D643, https://doi.org/10.1093/nar/gkaa978, 2021.

Boiteau, R. M., Mende, D. R., Hawco, N. J., McIlvin, M. R., Fitzsimmons, J. N., Saito, M. A., Sedwick, P. N., DeLong, E. F., and Repeta, D. J.: Siderophore-based microbial adaptations to iron scarcity across the eastern Pacific Ocean, Proc. Natl. Acad. Sci., 113, 14237–14242, https://doi.org/10.1073/pnas.1608594113, 2016.

Boiteau, R. M., Till, C. P., Coale, T. H., Fitzsimmons, J. N., Bruland, K. W., and Repeta, D. J.: Patterns of iron and siderophore distributions across the California Current System, Limnol. Oceanogr., 64, 376–389, https://doi.org/10.1002/lno.11046, 2019.

Buck, K. N., Lohan, M. C., Berger, C. J. M., and Bruland, K. W.: Dissolved iron speciation in two distinct river plumes and an estuary: Implications for riverine iron supply, Limnol. Oceanogr., 52, 843–855, https://doi.org/10.4319/lo.2007.52.2.0843, 2007.

Buck, K. N., Sohst, B., and Sedwick, P. N.: The organic complexation of dissolved iron along the U.S. GEOTRACES (GA03) North Atlantic Section, Deep. Res. Part II Top. Stud. Oceanogr., 116, 152–165, https://doi.org/10.1016/j.dsr2.2014.11.016, 2015.

Buck, K. N., Sedwick, P. N., Sohst, B., and Carlson, C. A.: Organic complexation of iron in the eastern tropical South Pacific: Results from US GEOTRACES Eastern Pacific Zonal Transect (GEOTRACES cruise GP16), Mar. Chem., 201, 229–241, https://doi.org/10.1016/j.marchem.2017.11.007, 2018.

Bundy, R. M., Abdulla, H. A. N., Hatcher, P. G., Biller, D. V., Buck, K. N., and Barbeau, K. A.: Iron-binding ligands and humic substances in the San Francisco Bay estuary and estuarine-influenced shelf regions of coastal California, Mar. Chem., 173, 183–194, https://doi.org/10.1016/j.marchem.2014.11.005, 2015.

Bundy, R. M., Boiteau, R. M., McLean, C., Turk-Kubo, K. A., McIlvin, M. R., Saito, M. A., Mooy, B. A. Van, and Repeta, D. J.: Distinct Siderophores Contribute to Iron Cycling in the Mesopelagic at Station ALOHA, Front. Mar. Sci., 1–15, https://doi.org/10.3389/fmars.2018.00061, 2018.

Butler, A.: Marine siderophores and microbial iron mobilization., Biometals, 18, 369–374, https://doi.org/10.1007/s10534-005-3711-0, 2005.

Butler, A. and Theisen, R. M.: Iron(III)-siderophore coordination chemistry: Reactivity of marine

470   siderophores., Coord. Chem. Rev., 254, 288–296, https://doi.org/10.1016/j.ccr.2009.09.010, 2010.

471   Callahan, B. J., McMurdie, P. J., Rosen, M. J., Han, A. W., Johnson, A. J. A., and Holmes, S. P.: DADA2:
472   High-resolution sample inference from Illumina amplicon data, Nat. Methods, 13, 581–583,
473   https://doi.org/10.1038/nmeth.3869, 2016.

474   Carmichael, J. R., Zhou, H., and Butler, A.: A suite of asymmetric citrate siderophores isolated from a marine
475   Shewanella species, J. Inorg. Biochem., 198, 1–6, https://doi.org/10.1016/j.jinorgbio.2019.110736, 2019.

476   Cowen, J. P. and Bruland, K. W.: Metal deposits associated with bacteria: implications for Fe and Mn marine
477   biogeochemistry, Deep Sea Res. Part A. Oceanogr. Res. Pap., 32, 253–272, https://doi.org/10.1016/0198-
478   0149(85)90078-0, 1985.

479   Cowen, J. P., Massoth, G. J., and Feely, R. A.: Scavenging rates of dissolved manganese in a hydrothermal
480   vent plume, Deep Sea Res. Part A. Oceanogr. Res. Pap., 37, 1619–1637, https://doi.org/10.1016/0198-
481   0149(90)90065-4, 1990.

482   Crowley, D. E., Wang, Y. C., Reid, C. P. P., and Szaniszlo, P. J.: Mechanisms of iron acquisition from
483   siderophores by microorganisms and plants, Plant Soil, 130, 179–198, 1991.

484   Fishwick, M. P., Sedwick, P. N., Lohan, M. C., Worsfold, P. J., Buck, K. N., Church, T. M., and Ussher, S.
485   J.: The impact of changing surface ocean conditions on the dissolution of aerosol iron, Global Biogeochem.
486   Cycles, 28, 1235–1250, https://doi.org/10.1002/2014GB004921, 2014.

487   Fitzsimmons, J. N., John, S. G., Marsay, C. M., Hoffman, C. L., Nicholas, S. L., Toner, B. M., German, C.
488   R., and Sherrell, R. M.: Iron persistence in the distal hydrothermal plume supported by dissolved – particulate
489   exchange, Nat. Geosci., 10, 1–8, https://doi.org/10.1038/ngeo2900, 2017.

490   Gu, H., Sun, Q., Luo, J., Zhang, J., and Sun, L.: A First Study of the Virulence Potential of a Bacillus subtilis
491   Isolate From Deep-Sea Hydrothermal Vent, Front. Cell. Infect. Microbiol., 9, 1–14,
492   https://doi.org/10.3389/fcimb.2019.00183, 2019.

493   Hawkes, J. A., Gledhill, M., Connelly, D. P., and Achterberg, E. P.: Characterisation of iron binding ligands
494   in seawater by reverse titration, Anal. Chim. Acta, 766, 53–60, https://doi.org/10.1016/j.aca.2012.12.048,
495   2013a.

496   Hawkes, J. A., Connelly, D. P., Gledhill, M., and Achterberg, E. P.: The stabilisation and transportation of
497   dissolved iron from high temperature hydrothermal vent systems, Earth Planet. Sci. Lett., 375, 280–290,
498   https://doi.org/10.1016/j.epsl.2013.05.047, 2013b.

499   Hider, R. C. and Kong, X.: Chemistry and biology of siderophores, Nat. Prod. Rep., 27, 637–657,
500   https://doi.org/10.1039/b906679a, 2010.

501   Hoffman, C. L., Nicholas, S. L., Ohnemus, D. C., Fitzsimmons, J. N., Sherrell, R. M., German, C. R., Heller,
502   M. I., Lee, J. mi, Lam, P. J., and Toner, B. M.: Near-field iron and carbon chemistry of non-buoyant
503   hydrothermal plume particles, Southern East Pacific Rise 15°S, Mar. Chem., 201, 183–197,
504   https://doi.org/10.1016/j.marchem.2018.01.011, 2018.

505   Hoffman, C. L., Schladweiler, C., Seaton, N. C. A., Nicholas, S. L., Fitzsimmons, J., Sherrell, R. M., German,
506   C. R., Lam, P., and Toner, B. M.: Diagnostic morphology and solid-state chemical speciation of
507   hydrothermally derived particulate Fe in a long-range dispersing plume, ACS Earth Sp. Chem., 4, 1831–
508   1842, https://doi.org/10.1021/acsearthspacechem.0c00067, 2020.

509   Homann, V. V, Sandy, M., Tincu, J. A., Templeton, A. S., Tebo, B. M., and Butler, A.: Loihichelins A - F ,
510   a Suite of Amphiphilic Siderophores Produced by the Marine Bacterium Halomonas LOB-5, J. Nat. Prod.,
511   72, 884–888, 2009.

512   Kato, C. and Nogi, Y.: Correlation between phylogenetic structure and function : examples from deep-sea

Shewanella, 35, 223–230, 2001.

Kelley, D. S. and Shank, T. M.: Hydrothermal systems: A decade of discovery in slow spreading environments, Geophys. Monogr. Ser., 188, 369–407, https://doi.org/10.1029/2010GM000945, 2010.

Kulmer, W. and Ingalls, A. E.: The R Journal: Tidy Data Neatly Resolves Mass-Spectrometry's Ragged Arrays, R J., 2022.

Lauderdale, J. M., Braakman, R., Forget, G., Dutkiewicz, S., and Follows, M. J.: Microbial feedbacks optimize ocean iron availability, Proc. Natl. Acad. Sci. U. S. A., 117, 4842–4849, https://doi.org/10.1073/pnas.1917277117, 2020.

Li, M., Toner, B. M., Baker, B. J., Breier, J. a, Sheik, C. S., and Dick, G. J.: Microbial iron uptake as a mechanism for dispersing iron from deep-sea hydrothermal vents., Nat. Commun., 5, 3192, https://doi.org/10.1038/ncomms4192, 2014.

Lough, A. J. M., Tagliabue, A., Demasy, C., Resing, J. A., Mellett, T., Wyatt, N. J., and Lohan, M. C.: The impact of hydrothermal vent geochemistry on the addition of iron to the deep ocean, Biogeosciences Discuss., [preprint], 1–23, https://doi.org/10.5194/bg-2022-73, 2022.

Manck, L. E., Park, J., Tully, B. J., Poire, A. M., Bundy, R. M., Dupont, C. L., and Barbeau, K. A.: Petrobactin, a siderophore produced by Alteromonas, mediates community iron acquisition in the global ocean, ISME J., 16, 358–369, https://doi.org/10.1038/s41396-021-01065-y, 2022.

Martinez, J. S., Carter-Franklin, J. N., Mann, E. L., Martin, J. D., Haygood, M. G., and Butler, A.: Structure and membrane affinity of a suite of amphiphilic siderophores produced by a marine bacterium, Proc. Natl. Acad. Sci. U. S. A., 100, 3754–3759, https://doi.org/10.1073/pnas.0637444100, 2003.

Mellett, T., Albers, J. B., Santoro, A., Wang, W., Salaun, P., Resing, J., Lough, A. J. ., Tagliabue, A., Lohan, M., Bundy, R. M., and Buck, K. N.: Particle exchange mediated by organic ligands in incubation experiments of hydrothermal vent plumes along the mid-Atlantic Ridge, n.d.

Moore, L. E., Heller, M. I., Barbeau, K. A., Moffett, J. W., and Bundy, R. M.: Organic complexation of iron by strong ligands and siderophores in the eastern tropical North Pacific oxygen deficient zone, Mar. Chem., 236, 104021, https://doi.org/10.1016/j.marchem.2021.104021, 2021.

Omanović, D., Garnier, C., and Pižeta, I.: ProMCC: An all-in-one tool for trace metal complexation studies, Mar. Chem., 173, 25–39, https://doi.org/10.1016/j.marchem.2014.10.011, 2015.

Parada, A. E., Needham, D. M., and Fuhrman, J. A.: Every base matters: Assessing small subunit rRNA primers for marine microbiomes with mock communities, time series and global field samples, Environ. Microbiol., 18, 1403–1414, https://doi.org/10.1111/1462-2920.13023, 2016.

Park, J., Durham, B. P., Key, R. S., Groussman, R. D., Pinedo-Gonzalez, P., Hawco, N. J., John, S. G., Carlson, M. C. G., Lindell, D., Juranek, L., Ferrón, S., Ribalet, F., Armbrust, E. V., Ingalls, A. E., and Bundy, R. M.: Siderophore production and utilization by microbes in the North Pacific Ocean, bioRxiv, 2022.02.26.482025, https://doi.org/10.1101/2022.02.26.482025, 2022.

Park, J., Durham, B. P., Key, R. S., Groussman, R. D., Pinedo-Gonzalez, P., Hawco, N. J., John, S. G., Carlson, M. C. G., Lindell, D., Juranek, L., Ferrón, S., Ribalet, F., Armbrust, E. V., Ingalls, A. E., and Bundy, R. M.: Siderophore production and utilization by microbes in the North Pacific Ocean, Limnol. Oceanogr., 2022.02.26.482025, https://doi.org/10.1002/lno.12373, 2023.

Quast, C., Pruesse, E., Yilmaz, P., Gerken, J., Schweer, T., Yarza, P., Peplies, J., and Glöckner, F. O.: The SILVA ribosomal RNA gene database project: Improved data processing and web-based tools, Nucleic Acids Res., 41, 590–596, https://doi.org/10.1093/nar/gks1219, 2013.

Resing, J. a., Sedwick, P. N., German, C. R., Jenkins, W. J., Moffett, J. W., Sohst, B. M., and Tagliabue, A.:

556 Basin-scale transport of hydrothermal dissolved metals across the South Pacific Ocean, Nature, 523, 200–
557 203, https://doi.org/10.1038/nature14577, 2015.

558 Ruttkies, C., Schymanski, E. L., Wolf, S., Hollender, J., and Neumann, S.: MetFrag relaunched: incorporating
559 strategies beyond in silico fragmentation, J. Cheminform., 8, 1–16, https://doi.org/10.1186/s13321-016-
560 0115-9, 2016.

561 Sander, S. G. and Koschinsky, A.: Metal flux from hydrothermal vents increased by organic complexation,
562 Nat. Geosci., 4, 145–150, https://doi.org/10.1038/ngeo1088, 2011.

563 Sandy, M. and Butler, A.: Microbial iron acquisition: marine and terrestrial siderophores., Chem. Rev., 109,
564 4580–95, https://doi.org/10.1021/cr9002787, 2009.

565 Santoro, A. E., Casciotti, K. L., and Francis, C. A.: Activity, abundance and diversity of nitrifying archaea
566 and bacteria in the central California Current, Environ. Microbiol., 12, 1989–2006,
567 https://doi.org/10.1111/j.1462-2920.2010.02205.x, 2010.

568 Sorokina, M., Merseburger, P., Rajan, K., Yirik, M. A., and Steinbeck, C.: COCONUT online: Collection of
569 Open Natural Products database, J. Cheminform., 13, 1–13, https://doi.org/10.1186/s13321-020-00478-9,
570 2021.

571 Stephens, B. M., Opalk, K., Petras, D., Liu, S., Comstock, J., Aluwihare, L. I., Hansell, D. A., and Carlson,
572 C. A.: Organic Matter Composition at Ocean Station Papa Affects Its Bioavailability, Bacterioplankton
573 Growth Efficiency and the Responding Taxa, Front. Mar. Sci., 7, https://doi.org/10.3389/fmars.2020.590273,
574 2020.

575 Sumner, L. W., Amberg, A., Barrett, D., Beale, M. H., Beger, R., Daykin, C. A., Fan, T. W.-M., Fiehn, O.,
576 Goodacre, R., Griffin, J. L., Hankemeier, T., Hardy, N., Harnly, J., Higashi, R., Kopka, J., Lane, A. N.,
577 Lindon, J. C., Marriott, P., Nicholls, A. W., Reily, M. D., Thaden, J. J., and Viant, M. R.: Proposed minimum
578 reporting standards for chemical analysis, Metabolomics, 3, 211–221, https://doi.org/10.1007/s11306-007-
579 0082-2, 2007.

580 Tagliabue, A., Bowie, A. R., Boyd, P. W., Buck, K. N., Johnson, K. S., and Saito, M. A.: The integral role
581 of iron in ocean biogeochemistry, Nature, 543, 51–59, https://doi.org/10.1038/nature21058, 2017.

582 Toner, B. M., Fakra, S. C., Manganini, S. J., Santelli, C. M., Marcus, M. a., Moffett, J. W., Rouxel, O.,
583 German, C. R., and Edwards, K. J.: Preservation of iron(II) by carbon-rich matrices in a hydrothermal plume,
584 Nat. Geosci., 2, 197–201, https://doi.org/10.1038/ngeo433, 2009.

585 Tortell, P. D., Maldonado, M. T., and Price, N. M.: The role of heterotrophic bacteria in iron-limited ocean
586 ecosystems, Nature, 383, 330–332, https://doi.org/10.1038/383330a0, 1996.

587 Vraspir, J. M. and Butler, A.: Chemistry of marine ligands and siderophores., Ann. Rev. Mar. Sci., 1, 43–63,
588 https://doi.org/10.1146/annurev.marine.010908.163712, 2009.

589 Waska, H., Koschinsky, A., Ruiz Chancho, M. J., and Dittmar, T.: Investigating the potential of solid-phase
590 extraction and Fourier-transform ion cyclotron resonance mass spectrometry (FT-ICR-MS) for the isolation
591 and identification of dissolved metal-organic complexes from natural waters, Mar. Chem., 173, 78–92,
592 https://doi.org/10.1016/j.marchem.2014.10.001, 2015.

593

Figures and Tables

596
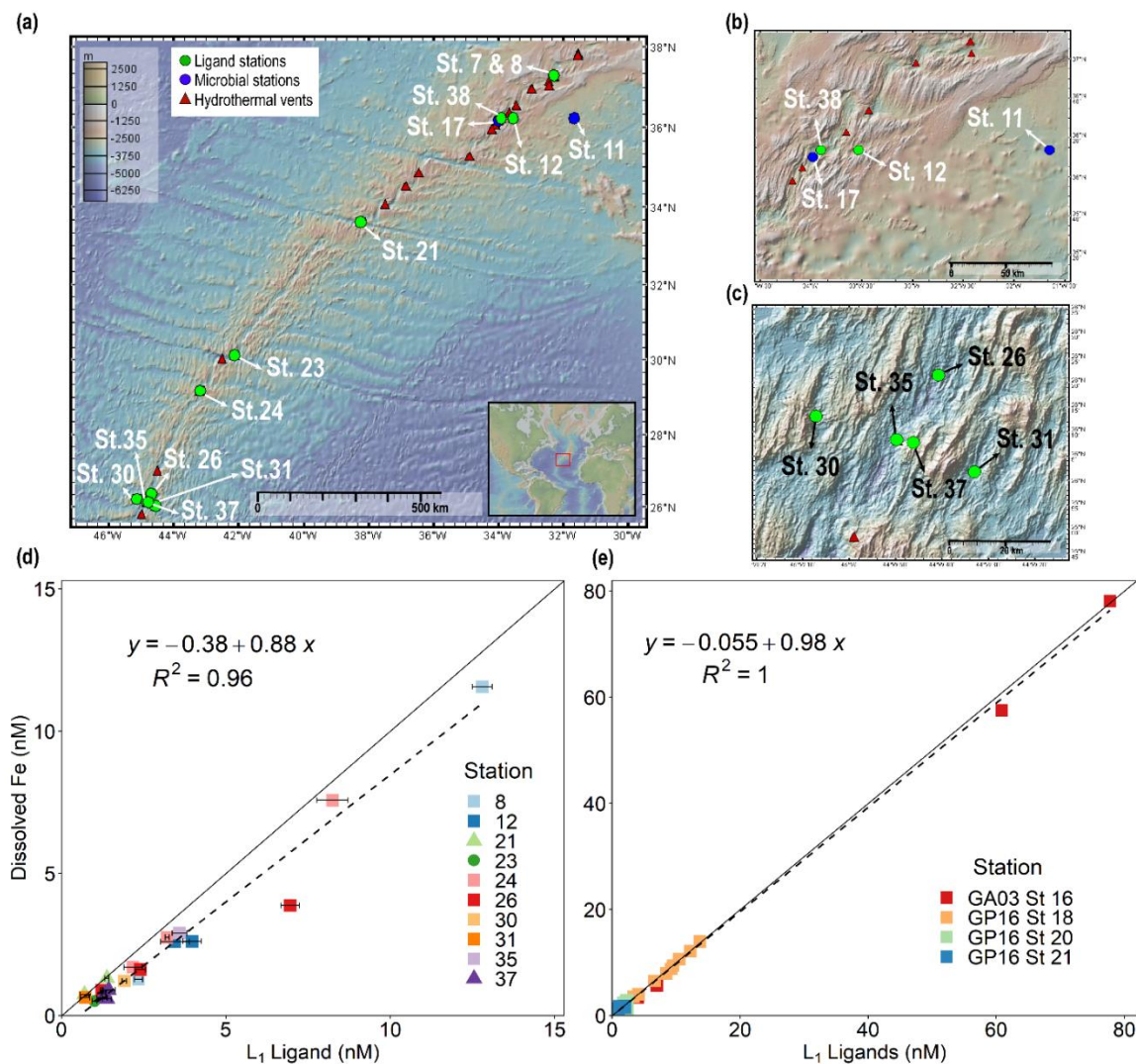
Figure 1. Dissolved iron is strongly correlated with L₁ iron-binding ligands in diverse hydrothermal systems. (a) Station map showing the 11 sites investigated along the MAR. Known hydrothermal vents are marked as red triangles(Beaulieu and Szafrański, 2020). Two expanded inset maps for (b) Rainbow and (c) TAG hydrothermal vent fields. For additional information about vent site characteristics refer to **Table 1**. (d) dFe versus L₁ iron-binding ligands at each vent site in this study showing a ~1:1 correlation (m= 0.88, R^2 = 0.96) with dFe in neutrally-buoyant plumes along the MAR. (e) dFe versus L₁ ligands from previous studies over the ridge axis and ~80 km from ridge axis in the Southern East Pacific Rise hydrothermal plume(Buck et al., 2018), and over TAG hydrothermal vent field(Buck et al., 2015). The solid black lines in (d) and (e) are the 1:1 ratio line between dFe and ligand concentrations, and dashed lines show the linear regression for the corresponding data. Square symbols refer to spreading centers, triangles refer to fracture zones, and

607   circles refer to alkaline vents. Error bars represent the 95% confidence interval of the data fit as calculated

608   by ProMCC(Omanović et al., 2015). The map was created using GeoMapApp version 3.6.14.

609

610
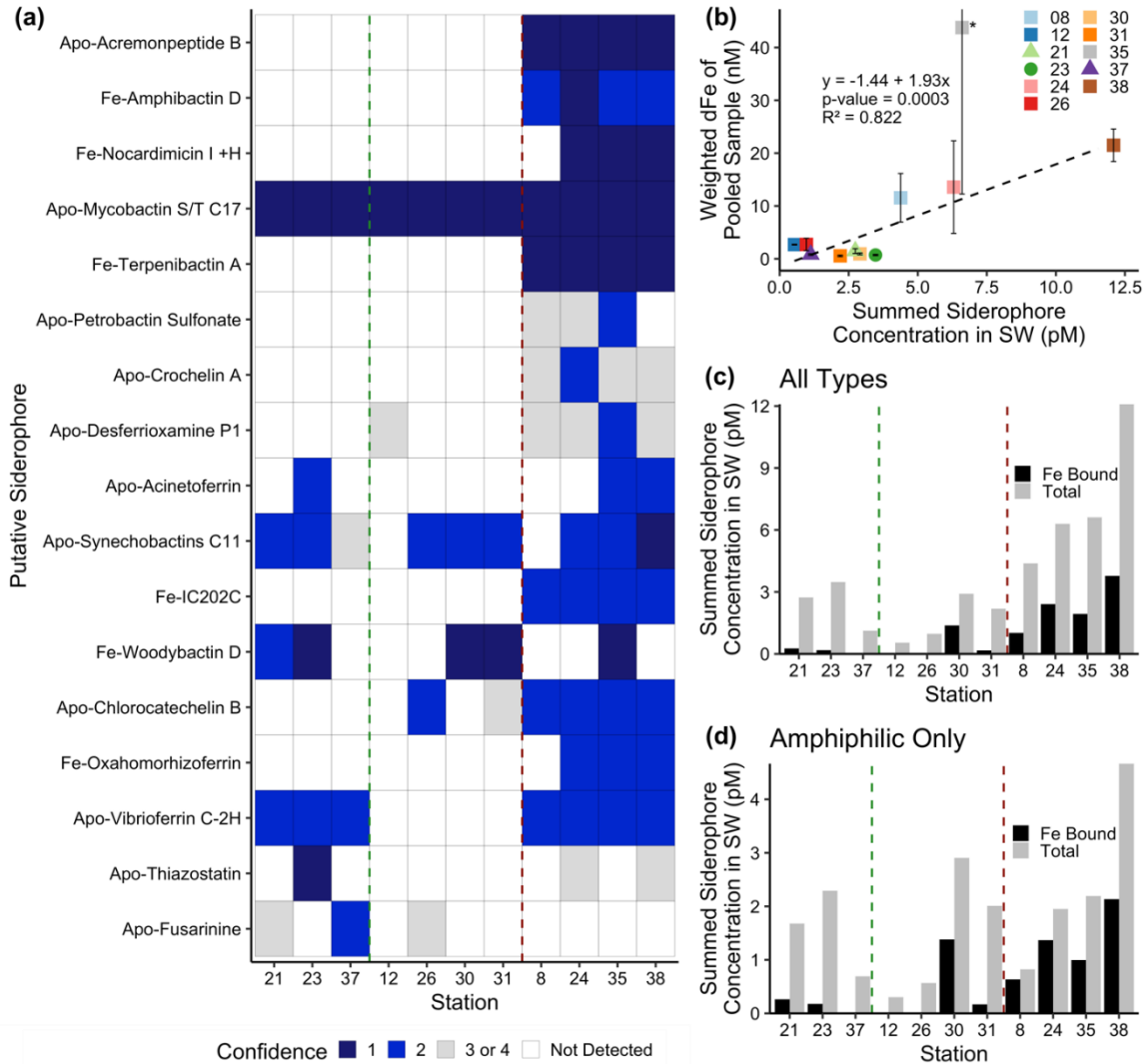
611

612

613 **Figure 2**. **Siderophore presence in hydrothermal plumes along the MAR.** (a) Heat map of confidence
614 levels 1-2 (blue gradient, 1 = highest confidence). Gray boxes indicate a detection with lower confidence (see
615 Methods), and white boxes indicate no detection at those sites. The y-axis is ordered from top to bottom in
616 terms of descending mass of the apo (without Fe) form of the siderophore. (b) Model II ordinary least squares
617 regression on dFe versus summed siderophore concentrations (of detections in Fig. 2b), calculated from peak
618 areas, at each site. Since the siderophore analysis was performed on pooled samples, the dFe values in the
619 regression are weighted values based on measured dFe and volume of each constituent of the pooled sample.
620 The vertical error bars represent the standard deviation of dFe of the constituents. TAG (St. 35) — denoted
621 by the asterisk — was not included in the regression due to its large range of dFe values and outlier behavior.
622 (c-d) Fe bound versus total summed concentration of (c) all types of siderophores and (d) amphiphilic
623 siderophores at each station. The vertical green lines separate fracture/diffuse sites from off-axis sites and
624 vertical red lines separate off-axis from on-axis sites as defined in Table 1. Symbols follow Fig. 1.

625
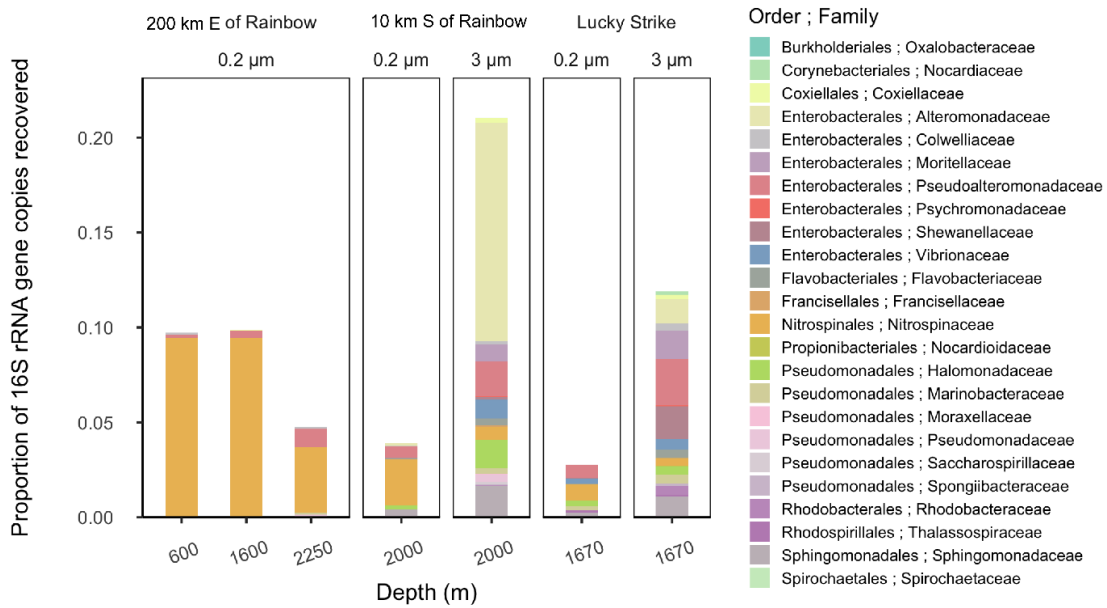
626

627

628   **Figure 3. Relative abundance of putative siderophore-producing taxa.** Bar height indicates the proportion

629   of 16S rRNA genes recovered in each sample, separated by depth from water surface, filter size fraction, and

630   site location. Colors correspond to taxonomy. Genera found in MAR vent microbial communities with

631   members in the antismash database predicted to produce siderophores are depicted at the family level.

632

633 **Table 1. Characteristics of sample locations along the Mid Atlantic Ridge.**

Vent Names	Abbr.	Station	Geology	Host rock	Vent type	Spreading rate (mm/yr)	Summed putative siderophore concentration (pM)	Summed Siderophore concentration/ L_1 ligand (%)*
Lucky Strike	LS	7/8	Spreading Center	gabbro	Black smoker	20.2	4.38	0.034-0.19
33 km E of Rainbow	CER	12	Spreading Center	-	-	-	0.537	0.013-0.017
Rainbow	R	38	Spreading Center	ultramafic	Black smoker	20.6	12.1	*n.a.*
Hayes Fracture Zone	HFZ	21	Fracture Zone	peridotites/gabbro	-	21.2	2.74	0.20-0.39
Lost City	LC	23	Fracture Zone	ultramafic/gabbro	Alkaline	22.6	3.47	0.27-0.35
Broken Spur	BS	24	Spreading Center	gabbro	Black smoker/diffuse	22.9	6.30	0.07-0.29
29 km N of TAG	CNT	26	Spreading Center	-	-	-	0.968	0.014-0.079
30 km W of TAG	CWT	30	Spreading Center	-	-	-	2.91	0.15
30 km E of TAG	CET	31	Spreading Center	-	-	-	2.19	0.31

| Trans-Atlantic Geotraverse | TAG | 35 | Spreading Center | gabbro | Black smoker | 23.6 | 6.61 | 0.18 |
| Low Temp Slope | LTS | 37 | - | - | Diffuse fluids | - | 1.13 | 0.079-0.087 |

Spreading rates along the Mid-Atlantic Ridge were gathered from the Interridge Database v3.4. Host rock groups were determined from previously discussed classifications(Bazylev, 1997; Kelley and Shank, 2010). Off-axis sites –33 km E of Rainbow, 29 km N of TAG, 30 km E of TAG, and 30 km W of TAG– were far-field locations of their respective vent field. Low Temp Slope was a diffuse-dominated site that was sampled for the first time as a part of this study. Summed putative siderophore concentrations and the percent of L_1 ligand are reported for compounds detected with at least confidence level 1 and 2 at one site. These values do not take into account typical extraction efficiencies of ENV columns for Fe-binding organics. Average L_1 ligand and siderophore concentrations can be viewed in **Table S3** and concentrations for individual siderophores can be observed in **Table S5**.

*The siderophore sample at each site was pooled from ligand samples, so the percentage of siderophores in the L_1 pool is presented as a range based on the range of L_1 concentrations at each site.

n.a.= unable to be determined

- = unknown

634
635